

Toward User-Friendly All-Sky Surface Longwave Downward Radiation from Space: General Scheme and Product

Yihan Du¹,^a Tianxing Wang,^{b,c,e} Yu Zhou,^a Husi Letu,^d Dahui Li,^b and Yuyang Xian^b

KEYWORDS:

Climate change;
Longwave radiation;
Radiation budgets

ABSTRACT: Longwave downward radiation (LWDR) is an important driving parameter in climate and hydrological models. Compared to traditional ground-based measurements, remote sensing has unique advantages in estimating global LWDR. However, for current remote sensing missions, as the typical available satellite-derived LWDR product with global coverage and hourly temporal resolution, the Clouds and the Earth's Radiant Energy System-Synoptic (CERES-SYN) top of atmosphere and surface fluxes and clouds has a low spatial resolution ($1^\circ \times 1^\circ$). There is still much room for improvement of the existing remote sensing LWDR products in terms of accuracy, spatiotemporal resolutions, and the ability to explain and quantify the changes of longwave radiation at various scales. To overcome these limitations, this paper developed a new global LWDR product with improved accuracy (RMSE $< 30 \text{ W m}^{-2}$ over the globe), high temporal resolution (hourly), and spatial resolution (5 km) based on Moderate Resolution Imaging Spectroradiometer (MODIS) measurements. It serves as a LWDR product within the Long-term Earth System spatiotemporally Seamless Radiation budget dataset (referred to as LessRad). As the first long-term high-resolution, spatiotemporally continuous LWDR product (2002–22, 1 h, 5 km), the LessRad reveals its advantages in studying the spatiotemporal variability of LWDR on finer scales. It also provides a valuable data source for various applications, such as analyzing land–atmosphere interactions and quantifying climate feedback, and thus is potentially helpful for understanding Earth's energy budget and dynamics.

SIGNIFICANCE STATEMENT: This study generated a long-term, high-resolution, spatiotemporally continuous longwave downward radiation product (2002–22, hourly, 5 km), known as LessRad LWDR. This product enables users to comprehensively and accurately assess the dynamics of global longwave downward radiation. In the context of global warming, accurate global estimation of longwave downward radiation is crucial for quantifying climate feedback. Our result showed that the user-friendly product provides a unique data foundation for the fine-scale studies of land radiation fluxes and related processes, even under complex terrain and various climatic conditions.

DOI: 10.1175/BAMS-D-23-0126.1

Corresponding author: Tianxing Wang, wangtx23@mail.sysu.edu.cn

Manuscript received 2 June 2023, in final form 16 March 2024, accepted 2 May 2024

© 2024 American Meteorological Society. This published article is licensed under the terms of the default AMS reuse license. For information regarding reuse of this content and general copyright information, consult the AMS Copyright Policy (www.ametsoc.org/PUBSReuseLicenses).

AFFILIATIONS: ^a Guangdong Provincial Key Laboratory of Geodynamics and Geohazards, School of Earth Sciences and Engineering, Sun Yat-Sen University, Zhuhai, China; ^b School of Geospatial Engineering and Science, Sun Yat-sen University and Southern Marine Science and Engineering Guangdong Laboratory (Zhuhai), Zhuhai, China; ^c Key Laboratory of Comprehensive Observation of Polar Environment (Sun Yat-sen University), Ministry of Education, Zhuhai, China; ^d State Key Laboratory of Remote Sensing Science, The Aerospace Information Research Institute, Chinese Academy of Sciences (CAS), Beijing, China; ^e Key Laboratory of Natural Resources Monitoring in Tropical and Subtropical Area of South China, Ministry of Natural Resources, Zhuhai, China

1. Introduction

Surface longwave downward radiation (LWDR) is a fundamental component of the surface radiation budget and serves as an important driving parameter in climate and hydrological models (Andrews et al. 2009; Colman 2015; DeAngelis et al. 2015; Loeb et al. 2021; Previdi and Liepert 2012). Accurately understanding LWDR is indispensable to the greenhouse effect, the global energy cycle, and climate feedback studies (Wild 2016). Compared to traditional ground-based measurements, remote sensing enables wide-scale and periodic coverage of both global and local regions, presenting a promising approach to meet the growing demand for LWDR applications.

The derivation of all-sky instantaneous LWDR has been extensively attempted and improved. To avoid the computational burden and input parameter requirements with radiation transfer models (Darnell et al. 1986; Frouin et al. 1988), parameterization methods were widely adopted to estimate LWDR (Cheng et al. 2019; Guo et al. 2018). Subsequently, the method of combining parameterization with top-of-atmosphere radiation or brightness temperature to estimate clear-sky LWDR has enhanced the physical basis of these estimations (Cheng et al. 2017; Wang and Liang 2009, 2010). With increasing attention to cloudy-sky LWDR retrieval (Forman and Margulis 2009; Gupta et al. 2010), cloud-base height or cloud-base temperature is a primary controlling factor of cloudy-sky LWDR but cannot be directly measured by optical sensors and needs to be estimated (Lin et al. 2022; Noh et al. 2017; Shao et al. 2023; Wang et al. 2018). To address this, some surrogated parameters are used to quantify the cloud contribution (Carmona et al. 2014; Duarte et al. 2006; Iziomon et al. 2003; Lhomme et al. 2007; Wang et al. 2020; Zhou and Cess 2001; Zhou et al. 2007).

Although satellite-based LWDR products have been widely applied in various disciplines, their coarse spatial resolutions (≥ 100 km) and insufficient accuracy make it difficult to detect changes in LWDR at smaller scales (Ma et al. 2014; Wang and Dickinson 2013). Having global coverage with high spatial resolutions, polar-orbiting satellites [such as Moderate Resolution Imaging Spectroradiometer (MODIS)] are considered the best data source for deriving LWDR with improved spatial scales (Liang et al. 2021; Nussbaumer and Pinker 2012). Nevertheless, the daily limited number and time inconsistency of instantaneous observations constrain their application. The Clouds and the Earth's Radiant Energy System-Synoptic (CERES-SYN), widely utilized as a long-term global remote sensing product, is specifically designed to accurately capture diurnal variations (Doelling et al. 2016; Rutan et al. 2015). However, it does suffer from low spatial resolution ($1^\circ \times 1^\circ$). The Global Land Surface Satellite (GLASS) suite continuously updates its LWDR products (Shunlin et al. 2023). GLASS-AVHRR (1981–2018) at 5-km resolution provides daily land-only LWDR, GLASS-MODIS (2000–20) at 1-km resolution

offers instantaneous LWDR, and GLASS-MODIS at 5-km resolution (2002–20) provides only daily LWDR. Additionally, some regional LWDR products can also be available based on geostationary satellites (Carrer et al. 2012; Letu et al. 2022; Yang et al. 2017). Reanalysis data are increasingly being used in global climate monitoring, with many of these datasets providing LWDR products (Gelaro et al. 2017; Kobayashi et al. 2015; Saha et al. 2014, 2010). ERA5 has the highest spatiotemporal resolution (ERA5 with ~ 31 km and 1 h, ERA5-Land with ~ 9 km and 1 h) among them (Hersbach et al. 2020; Muñoz-Sabater et al. 2021). However, their accuracy is limited in certain regions, such as the Tibetan Plateau, which is of significant interest to the scientific community. In this region, they underestimate by more than 25 W m^{-2} (Wang et al. 2021; Zhu et al. 2022).

Accurately capturing the diurnal variations of LWDR can provide a deeper understanding of large-scale climate change, and ecological and surface processes (Doelling et al. 2016; Forman and Margulis 2009). For most research and applications, the ideal resolution of LWDR is less than 10 km, and subdaily or even hourly (Bourassa et al. 2013; Xu et al. 2023). With the targeted improvement of our LWDR algorithms (Wang et al. 2023, 2020), this study intends to generate an all-sky global LWDR product (2002–22, hourly, 5 km) with reliable accuracy based on MODIS measurements. It serves as an LWDR product within the Long-term Earth System spatiotemporally Seamless Radiation budget dataset (referred to as LessRad).

2. Datasets

a. MOD/MYD06 data. MODIS is a widely used remote sensing satellite sensor, which provides instantaneous retrievals for various atmospheric, land, and ocean parameters (Platnick et al. 2017). In this study, the MOD06_L2/MYD06_L2 products were utilized to estimate the all-sky instantaneous LWDR. The datasets employed consisted of surface temperature (ST), cloud-top temperature (CTT), and cloud fraction (CF), with a spatial resolution of 5 km. The temporal coverage spans from 2002 to 2022.

b. Auxiliary data. The auxiliary data used in this study are the ERA5 reanalysis product. ERA5 provides high-quality reanalysis data for a range of surface and atmospheric parameters. The auxiliary data used for estimating instantaneous all-sky LWDR are ERA5 total column water vapor (TCWV) hourly data with a temporal resolution of 0.25° . Additionally, ERA5 LWDR hourly data with a resolution of 0.25° are utilized as prior knowledge for LWDR temporal upscaling. To ensure accuracy and reliability, these data were resampled to a resolution of 5 km and temporally interpolated to instantaneous every minute to match the MODIS measurement data.

c. Validation data. The validation data were collected from 292 sites distributed worldwide, covering a wide range of geographical regions and climate conditions. These ground measurement sites come from the following observation networks: Baseline Surface Radiation Network (BSRN) (Driemel et al. 2018), the National Tibetan Plateau Data Center (TPDC) (Ma et al. 2020), TOGA–Tropical Atmosphere Ocean (TOGA-TAO) (Mangum et al. 1994), AmeriFlux (Schmidt et al. 2012), Coordinated Energy and Water Cycle Observation Project (CEOP) (Tamagawa et al. 2008), AsiaFlux (Mizoguchi et al. 2009), and Heihe Watershed Allied Telemetry Experimental Research (HiWATER) (Li et al. 2013). Please note that the LWDR values from these site measurements have not been assimilated into ERA5 LWDR. Considering that each network has different temporal resolutions, all ground observation data are temporally averaged to hourly intervals (when the missing data are less than one-third in the corresponding period). The distribution of all sites is shown in Fig. 1. Detailed information about each site can be found in Table 1.

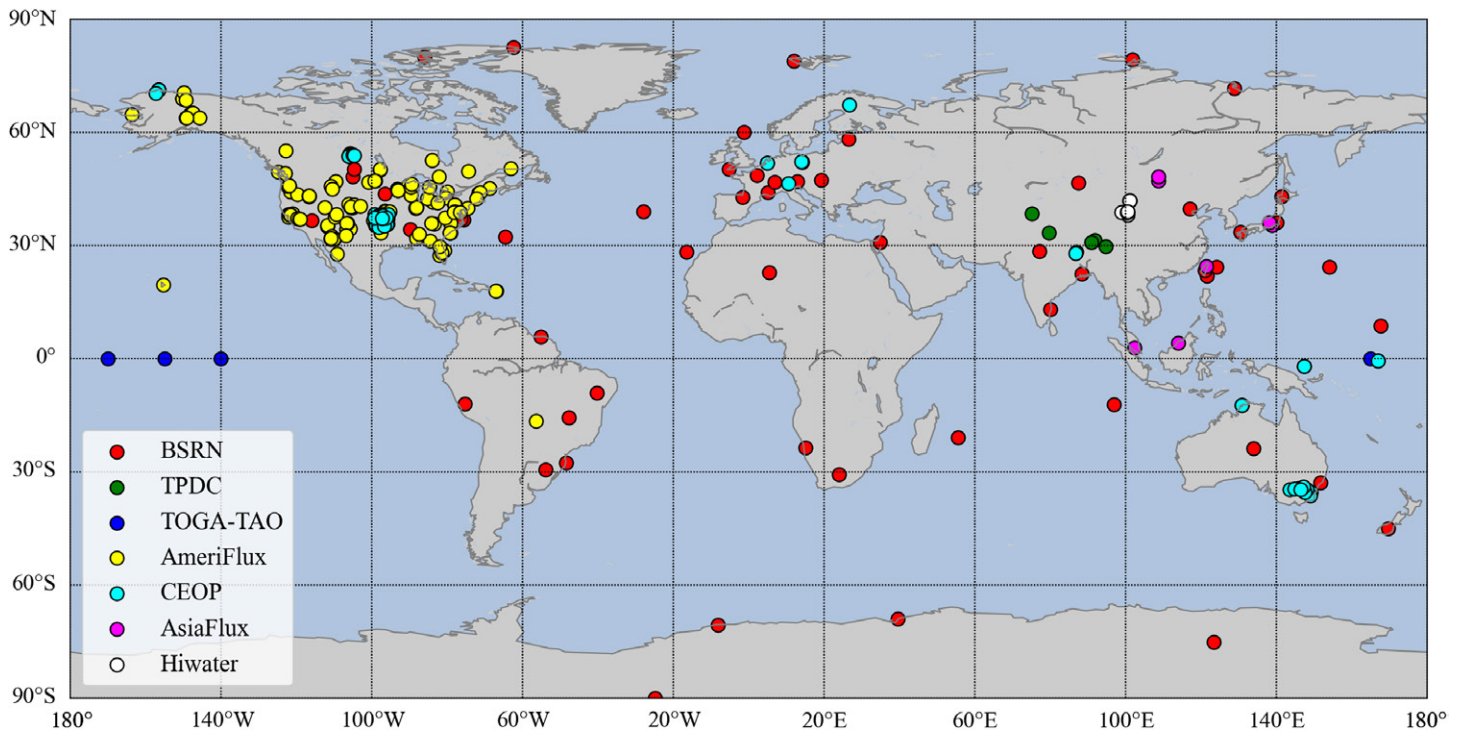


FIG. 1. Spatial distribution of the ground observation sites used in this study.

3. Processing methodology

The LWDR production algorithm consists of two parts, i.e., instantaneous LWDR calculation and temporal upscaling.

First, an improved version of parameterization only based on CTT, ST, and TCWV is employed to generate all-sky instantaneous LWDR (Letu et al. 2022; Wang et al. 2023, 2020). Specifically, a new representative training database is incorporated to improve the accuracy of the derived instantaneous all-sky LWDR and to reduce the relatively large errors of LWDR (flux range $< 150 \text{ W m}^{-2}$) under extremely cold and dry conditions; the corresponding parameterization coefficients of the refitted polynomial model are updated. The resulting instantaneous LWDR had an RMSE of less than 22 W m^{-2} and a bias of less than 0.5 W m^{-2} under all-sky conditions (Wang et al. 2023).

The cloud strongly modulates LWDR, and the cloudy thermal contribution is directly related to either the cloud-base temperature or height (Zhou and Cess 2001). However, optical remote sensing can only detect cloud-top information due to the opacity of the clouds. Therefore, many remote sensing missions provide CTT, which offers the possibility of calculating LWDR under cloudy sky. The all-sky LWDR is modeled as

$$\text{LWDR}_{\text{clr}} = A_0 + A_1 \times \text{ST}^{a_0} \times \ln(1 + \text{CWV})^{a_1} + A_2 \times \ln(1 + \text{CWV})^{a_2} + A_3 \times \ln(1 + \text{CWV})^{a_3}, \quad (1)$$

TABLE 1. Detailed information of ground observation sites used in this study.

Networks	Time range	Time resolution	No. of sites
AmeriFlux	2006, 2008, 2010, 2014, 2016, 2019	30 min	157
AsiaFlux	2006, 2008, 2010, 2014, 2016, 2019	30 min	7
BSRN	2006, 2008, 2010, 2014, 2016, 2019	1 min	64
CEOP	2006, 2008, 2010	30 min	43
TOGA-TAO	2008, 2010, 2014	2 min	4
TPDC	2006, 2008, 2010, 2014, 2016	1 h	5
HiWATER	2014	10 min	12

$$\text{LWDR}_{\text{cld}} = B0 + B1 \times \text{LWDR}_{\text{atm}} + B2 \times \text{CTT}^{b0} / \left[\ln(1 + \text{CWV})^{b1} + \ln(1 + \text{CWV})^{b2} + \ln(1 + \text{CWV})^{b3} \right], \quad (2)$$

$$\text{LWDR}_{\text{All-sky}} = (1 - \text{cf}) \times \text{LWDR}_{\text{clr}} + \text{LWDR}_{\text{cld}} \times \text{cf}, \quad (3)$$

where LWDR_{clr} is the clear-sky LWDR; A0, A1, A2, A3, a0, a1, a2, and a3, and B0, B1, B2, b0, b1, b2, and b3 are all fitting coefficients (Table 2); LWDR_{cld} is the cloudy-sky LWDR; LWDR_{atm} is the thermal contribution from the subcloud atmosphere, calculated using the same equation and coefficient; cf is the cloud fraction of pixels; and $\text{LWDR}_{\text{All-sky}}$ is the all-sky LWDR.

Then, considering the impact of abnormal or missing observations in instantaneous samples, the instantaneous LWDR is upscaled to an hourly scale (or any time scale) using the diurnal variation shape of LWDR from prior knowledge (Du et al. 2023). By taking into account the resolution and accuracy of existing products, although ERA5 still has limitations in local accuracy and diurnal variations, preventing it from being an ideal LWDR product, it possesses the advantages of global coverage, temporal continuity, and spatial uniformity. Different resolutions represent different LWDR trends. In preliminary tests, while CERES-SYN has made significant contributions in capturing the diurnal cycle, the spatial matching of a 1° resolution from CERES-SYN with a 5-km resolution from MODIS may introduce additional uncertainties and errors due to the significant difference in spatial scales. ERA5, on the other hand, can provide diurnal shape patterns similar to ground observations in most cases (Du et al. 2023). Therefore, we have chosen the ERA5 LWDR product as the prior information for temporal upscaling in this study. This method fully combines the high spatial resolution of polar-orbiting satellites with the excellent temporal performance of reanalysis data. Specifically, the difference between the MODIS instantaneous LWDR and the ERA5 LWDR of corresponding time was first calculated. Then, between each pair of consecutive MODIS overpass times, we combine the average of the differences with the ERA5 LWDR to obtain the LWDR curve of the new product.

The algorithm constructed for generating LessRad LWDR product with a 5-km spatial resolution and hourly temporal resolution is represented by the flowchart shown in Fig. 2. The input data include MODIS CTT, ST, and ERA5 TCWV, which are used to calculate the instantaneous LWDR. Additionally, ERA5 LWDR data are utilized as prior knowledge for temporal upscaling.

4. Features of LessRad LWDR

In this section, three characteristics of LessRad LWDR are presented: 1) currently, the only spatiotemporal continuous all-sky LWDR product (2002–22) with kilometer spatial resolution, hourly temporal resolution, and improved accuracy; 2) noticeable improvements in accuracy and spatial pattern at regional scales in challenging terrains and diverse climatic conditions; and 3) providing a feasible scheme and reference to generate high-resolution LWDR products at any temporal scales based on instantaneous measurements of a single remote sensing instrument (e.g., MODIS).

To better visualize and analyze the temporal trends of LWDR over the 21 years, this study divided the globe into different regions: the low-latitude zone (30°N–30°S), the midlatitude zone (30°–60°N and 30°–60°S), the Tibetan

TABLE 2. Coefficients of the parameterizations for the all-sky LWDR.

Clear-sky coefficients		Cloudy-sky coefficients	
A0	3.8902588	B0	36.9765
A1	0.00021458248	B1	0.868615
A2	0.86771970	B2	1.19126×10^{-5}
A3	44.400631	b0	2.89056
a0	2.4802001	b1	2.22786
a1	0.16513199	b2	-0.278429
a2	5.2873775	b3	-0.175044
a3	0.83203453		

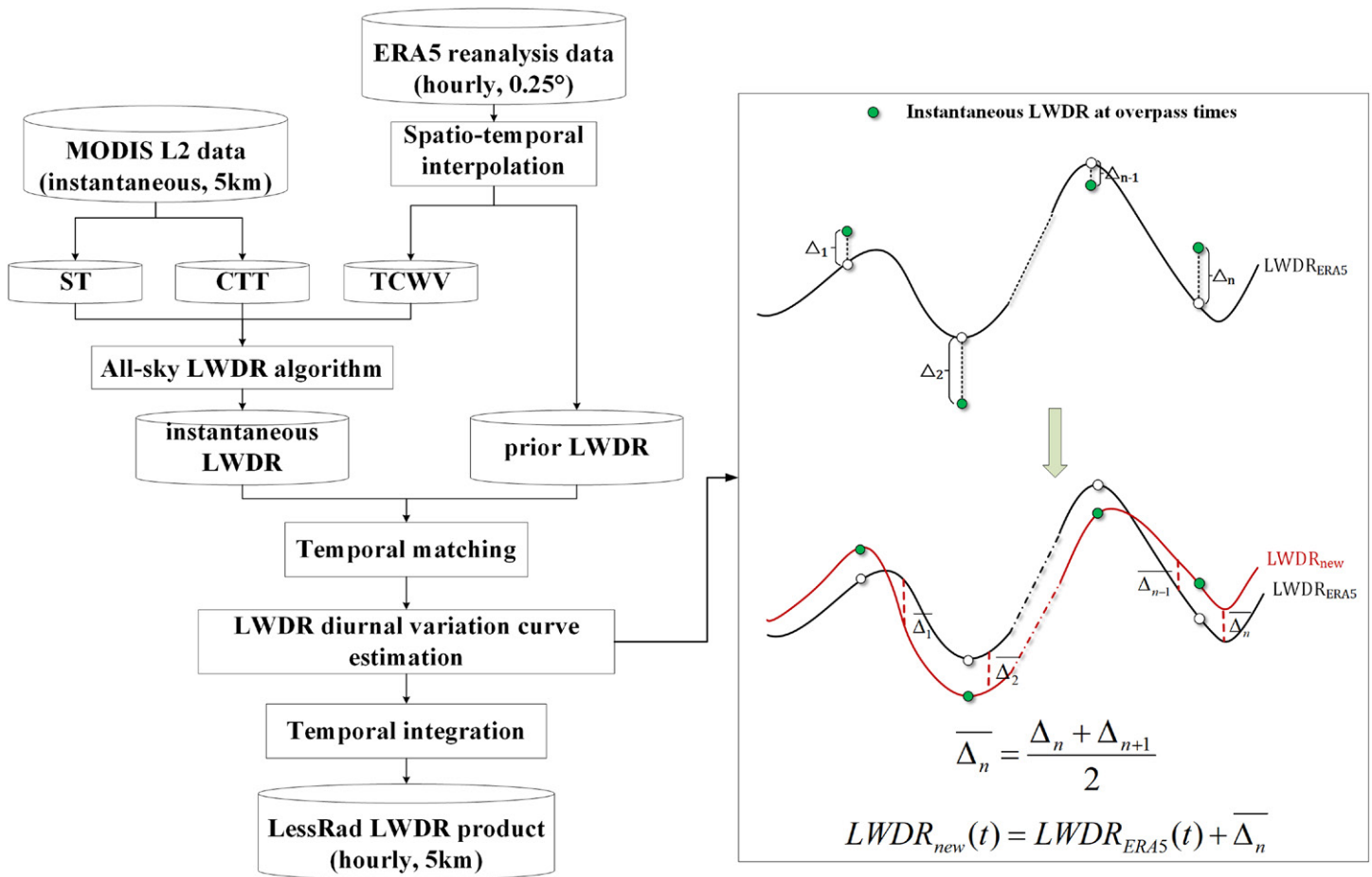


FIG. 2. Flowchart for generating LessRad LWDR product.

Plateau zone (20°–50°N and 60°–110°E), the Arctic zone (60°–90°N), and the Antarctic zone (60°–90°S). The Tibetan Plateau, the Antarctic, and the Arctics, known as Earth’s three poles, have complex climatic conditions and are considered typical areas highly sensitive to global climate change (DeConto and Pollard 2016; Hu et al. 2023; Screen and Simmonds 2010). Thus, these regions are selected as intensive areas for validation and analysis.

LessRad is developed based on the advanced all-weather instantaneous algorithm and temporal upscaling algorithm, which greatly minimizes the error propagation of invalid values and uncertainties of instantaneous LWDR to hourly scale LWDR estimation. We selected two well-known and temporally continuous global LWDR datasets, CERES-SYN and ERA5. The spatial details of LessRad were compared with them (Fig. 3). LessRad has a higher spatial resolution (0.05°) compared to the CERES-SYN (1°) and ERA5 (0.25°) products, implying that more details of LWDR variations can be successfully monitored. Moreover, unlike LessRad, in the area labeled “a” located in the Tibetan Plateau, both the ERA5 and CERES-SYN are considered to underestimate the LWDR, as validated in section 5. This could be attributed to the influence of spatial resolution, and the low-value areas appear larger than their actual extent due to the coarse spatial resolution. Similar phenomena also occur in other local regions.

Studying the temporal variations of long-term LWDR is crucial in the context of global warming. During the 21 years from 2002 to 2022, the monthly LWDR from all the datasets in each region consistently exhibits systematic LWDR variations from peaks to troughs on an annual basis (Fig. 4). This pattern of variation aligns with the annual seasonal changes; that is, LWDR reaches its peak during the summer season and reaches its lowest point during the spring and winter seasons. This seasonal variation in LWDR is particularly pronounced

00:00 on March 15, 2016

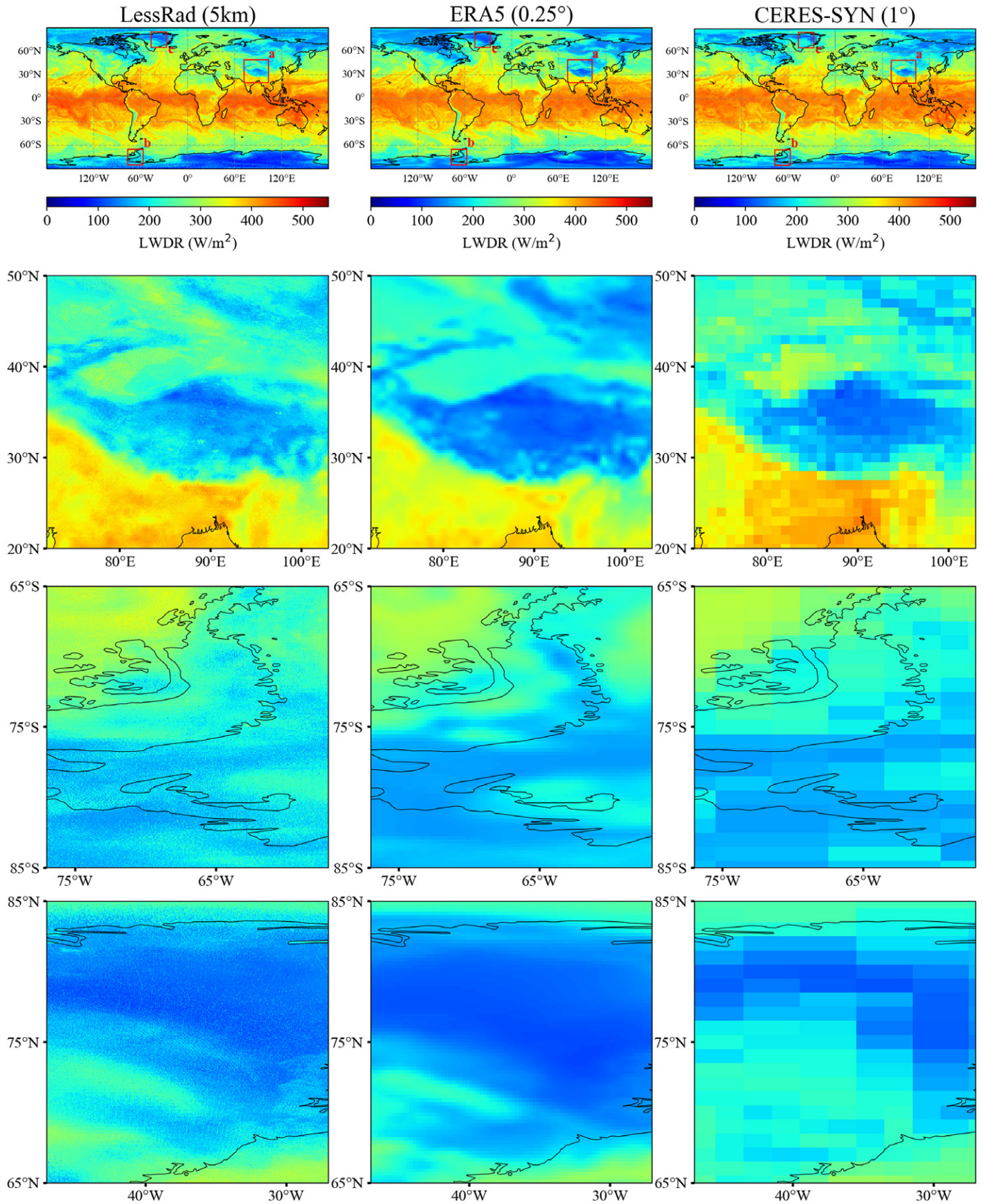


FIG. 3. Comparison of the LWDR from (left) LessRad-5 km, (center) ERA5-0.25°, and (right) CERES-SYN-1° at 0000 UTC 15 Mar 2016. The top row shows the global LWDR, while the second to fourth rows depict zoomed-in areas corresponding to labels a–c in the top row (their relative positions in the global map are indicated in the top row, located in the Tibetan Plateau, Antarctica, and the Arctic, respectively).

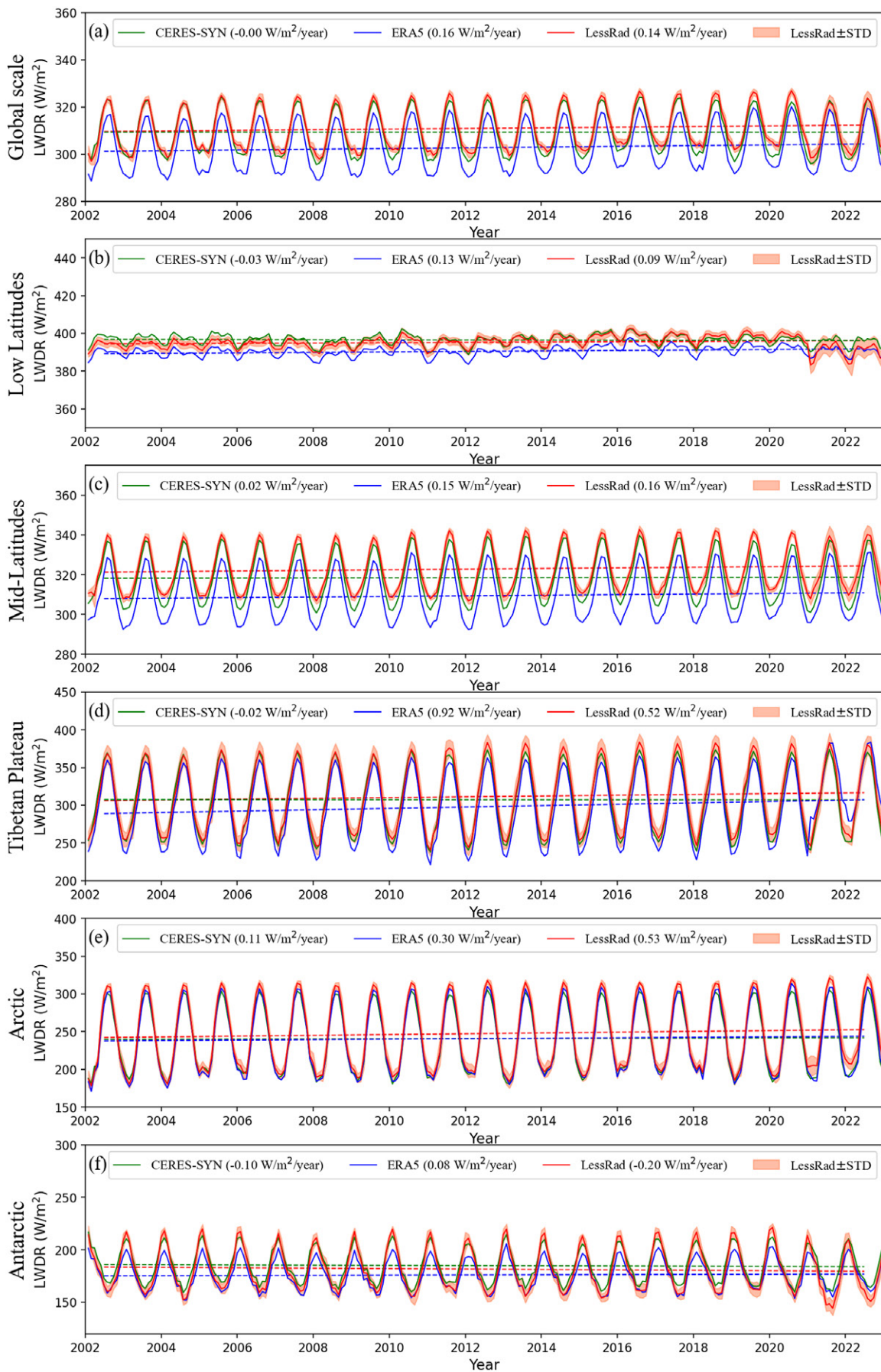


FIG. 4. Monthly time series and trends of CERES-SYN (green), ERA5 (blue), and LessRad (red), from 2002 to 2022 at (a) global scale, (b) low latitudes, (c) midlatitudes, (d) Tibetan Plateau, (e) Arctic, and (f) Antarctic. STD: monthly standard deviation for each product.

in the Tibetan Plateau and midlatitude regions. In low-latitude regions, the interannual variation amplitude of LWDR is approximately 20 W m^{-2} , which is the smallest among the studied regions.

Previously, according to the BSRN LWDR records from 1990 to 2014, Wild (2016) proposed that the LWDR has been increasing by $2.0 \text{ W m}^{-2} \text{ decade}^{-1}$ since the early 1990s. At the global scale, both LessRad and ERA5 show an increasing trend in LWDR. In contrast, the trends observed in CERES-SYN are less pronounced, which could be attributed to the potential limitations arising from its coarse resolution. Over the past two decades, ERA5 has exhibited a positive trend of $1.6 \text{ W m}^{-2} \text{ decade}^{-1}$, while LessRad shows a trend of $1.4 \text{ W m}^{-2} \text{ decade}^{-1}$, consistent with the trend of global warming caused by enhanced global greenhouse effects. Compared to other regions, the Tibetan Plateau and the Arctic exhibit the most pronounced trends in LWDR changes. According to the LessRad data, they show an increasing trend of 5.2 and $5.3 \text{ W m}^{-2} \text{ decade}^{-1}$, respectively, which aligns with the amplification effects of the Tibetan Plateau and the Arctic on global climate (Hu et al. 2023; Screen and Simmonds 2010).

The quantity and temporal distribution of MODIS instantaneous LWDR are insufficient to meet the requirement for continuous observations (as shown in Fig. 5). The radiative forcing of clouds contributes to more uncertainties in the LWDR, leading to more observations necessary to quantify the diurnal variation of LWDR. However, the instantaneous LWDR acquired from satellite data is limited by the overpass time, especially the polar-orbiting satellites can only acquire a limited number of instantaneous LWDR observations per day. Additionally, both anomalies and missing instantaneous samples can lead to a significant decrease in the accuracy and validity rate of LWDR temporal upscaling (Du et al. 2023). LessRad reduces the invalid values and uncertainties of temporal upscaling based on limited instantaneous LWDR samples, enabling a more temporally continuous LWDR that is closer to ground observations compared to other products. Additionally, LessRad modifies the underestimation of ERA5 and the errors introduced in the MODIS instantaneous LWDR estimation (Fig. 5).

To further compare the performance of different products under complex conditions, the hourly and daily LWDR comparisons of each product over the Tibetan Plateau for January 2016 and the entire year are shown in Fig. 6. ERA5 shows significant underestimation in LWDR over the Tibetan Plateau (detailed accuracy validation in section 5). However, its shape of the diurnal variation closely matches the ground observations, which is why we selected ERA5 as the prior knowledge. Although LessRad utilizes ERA5 LWDR diurnal variation

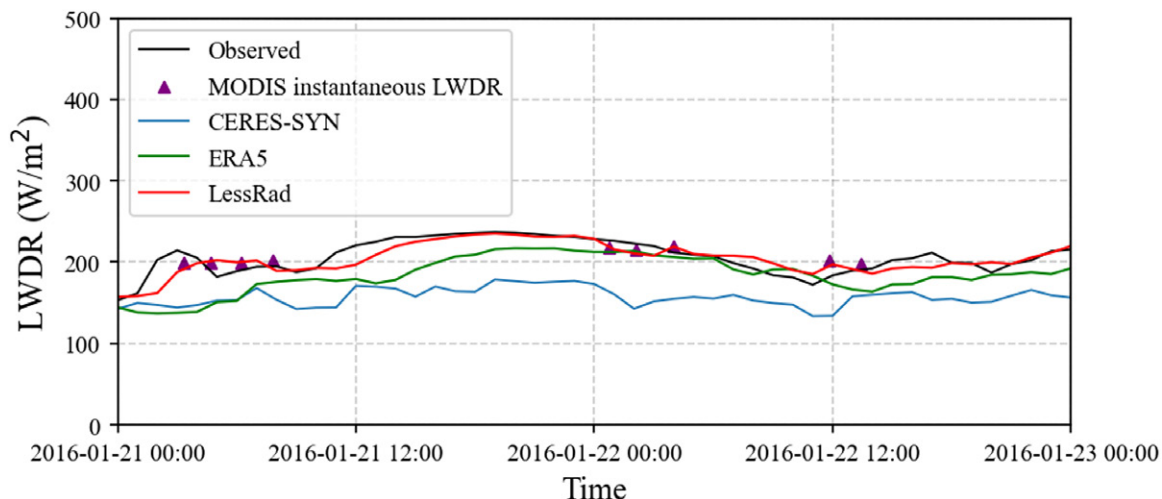


FIG. 5. Hourly LWDR from CERES-SYN (1°), ERA5 (0.25°), and LessRad (5 km), as well as MODIS instantaneous LWDR observations at the ground site of the Arctic (71.5862°N , 128.9188°E) on 21–22 Jan 2016.

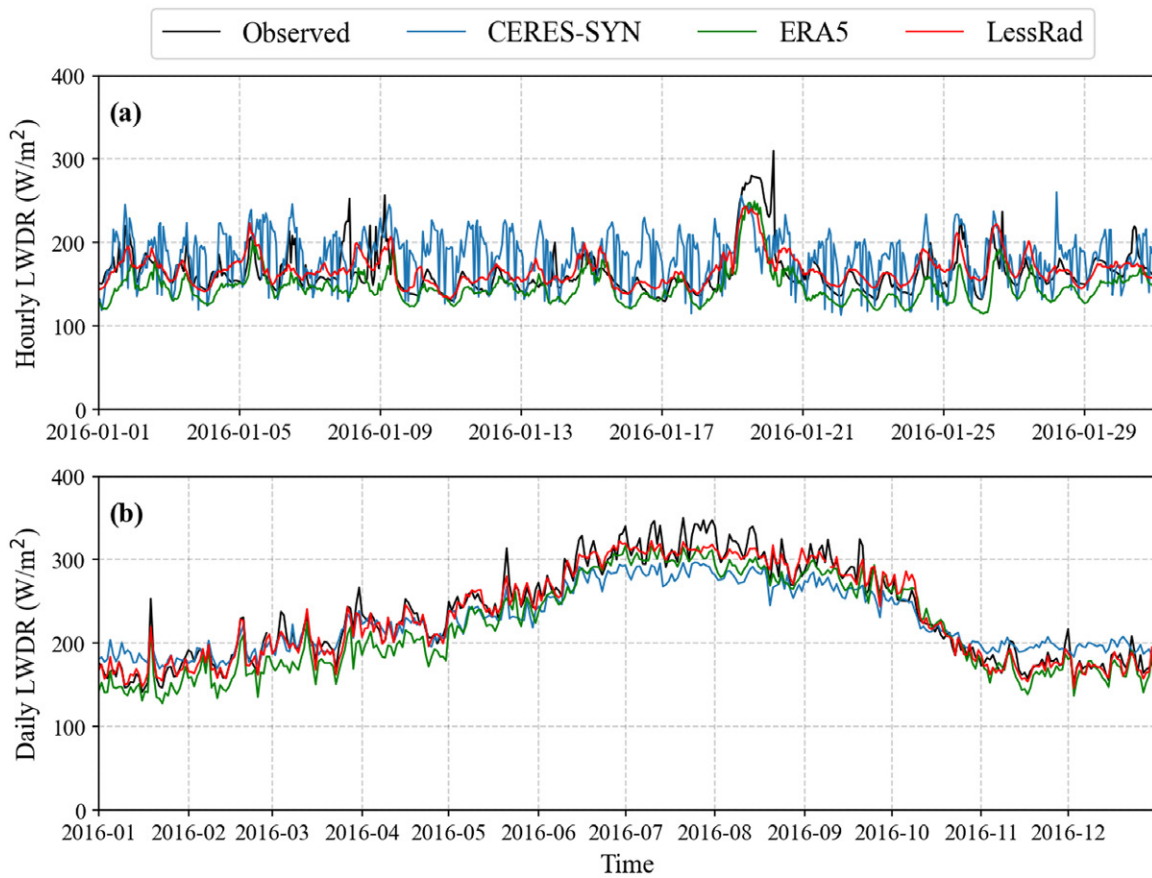


FIG. 6. (a) Hourly and (b) daily LWDR variations of CERES-SYN, ERA5, and LessRad, at the ground site of the Tibetan Plateau (28.36°N, 86.95°E). All products have been resampled to a scale of 1°.

shape as prior knowledge, it does not exhibit the same underestimation. Compared to ERA5 or CERES, LessRad provides significantly closer LWDR values to ground measurements. This demonstrates that even in regions with complex climates and terrains, LessRad can accurately capture diurnal variations of LWDR.

5. Validation and comparison

LessRad LWDR was first compared with ground observation data in different regions. Accuracy was evaluated using root-mean-square error (RMSE), mean bias error (MBE), and correlation coefficient (R). LessRad showed a high global performance with an R value of 0.91, an MBE of $5.5 W m^{-2}$, and an RMSE of $29.7 W m^{-2}$. This indicates that LessRad LWDR performs well at a high spatial resolution. In specific regions such as low latitudes, midlatitudes, the Tibetan Plateau, the Arctic, and the Antarctic, the product achieved R values of 0.90, 0.86, 0.90, 0.87, and 0.94, with MBE values of 1.4, 6.6, 1.7, 2.1, and $2.6 W m^{-2}$, and RMSE values of 21.4, 31.0, 32.0, 30.2, and $24.2 W m^{-2}$, respectively (Fig. 7).

To quantitatively validate the performance of LessRad LWDR, we also used CERES SYN and ERA5 products for comparison (Fig. 8). First, to ensure theoretical comparability among these products on global and regional scales, LessRad and ERA5 were aggregated to the spatial resolution of CERES-SYN ($1^\circ \times 1^\circ$). Validation based on ground measurements revealed that LessRad, CERES, and ERA5 show global RMSE values of 27.8, 30.8, and $29.6 W m^{-2}$, respectively. Moreover, not only at the global scale but also in different local regions, such as the Tibetan Plateau, the Arctic, the Antarctic, and midlatitudes, the accuracy of LessRad surpasses that of other products. In low-latitude regions, the accuracy of the three products is similar. Specifically, the deviations for LessRad, CERES,

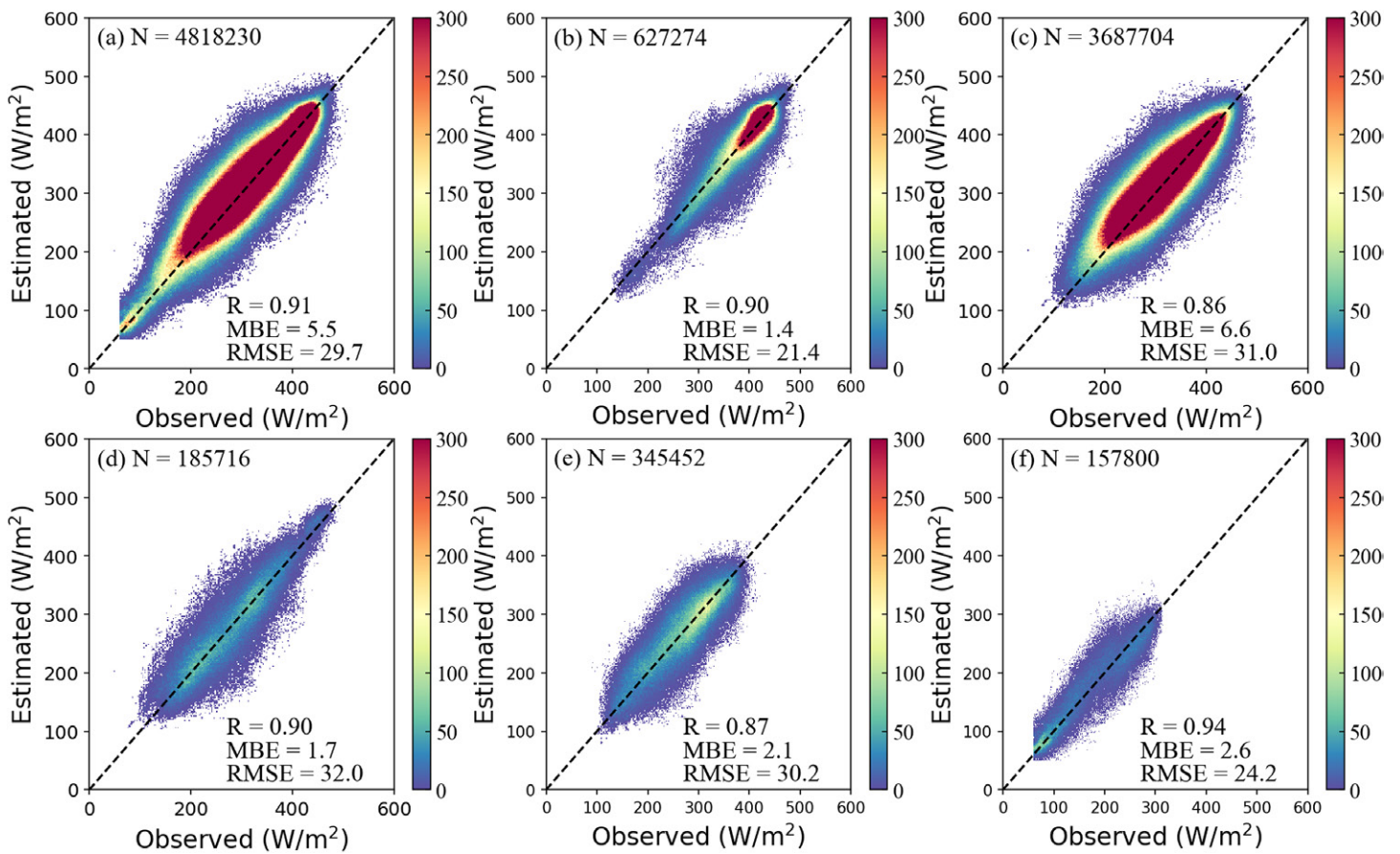


FIG. 7. Validation of LessRad LWDR (5 km) with ground-based measurements at (a) global scale, (b) low latitudes, (c) midlatitudes, (d) the Tibetan Plateau, (e) the Arctic, and (f) the Antarctic.

and ERA5 are 1.6, 0.2, and -4.6 W m^{-2} , respectively, while the corresponding RMSE values are 20.0, 21.4, and 19.5 W m^{-2} .

It is worth noting that ERA5 exhibits poor accuracy in certain regions, particularly in high-altitude areas such as the Tibetan Plateau. When compared to ground observations, ERA5 significantly underestimates LWDR, with an MBE value of -25.4 W m^{-2} and RMSE value of 39.4 W m^{-2} . In contrast, LessRad and CERES-SYN demonstrate MBE values of 1.4 and -9.6 W m^{-2} , and RMSE values of 29.5 and 35.4 W m^{-2} , respectively.

The differences in climate conditions, particularly the differences in cloud cover, water vapor, and temperature, which are closely related to LWDR, can result in distinct LWDR values and variations across different regions. Considering the impact of LWDR on climate change research, we compared the RMSEs of various products at all validation sites based on the Köppen–Geiger climate classification (Fig. 9). This classification is based on regional vegetation characteristics, temperature, and precipitation (Beck et al. 2023). The accuracy in different regions is consistent with Fig. 8. It can be observed that the selected validation sites cover most climatic types worldwide. Across various climatic types and sites, LessRad shows better or comparable accuracy to other products. In dry regions, LWDR is more likely to exhibit greater uncertainty.

In addition, LessRad improves the accuracy and shows a noticeable advantage in spatial resolution. The validation across nine major land cover types (Fig. 10) reveals that at a finer resolution (5 km), LessRad exhibits superior or comparable accuracy across various performance metrics compared to CERES-SYN (at 1° resolution) and ERA5 (at 0.25° resolution). This is attributed to the fact that at coarser spatial resolutions, the pixels may contain multiple land cover types (with different STs), thereby affecting the value of LWDR. With its

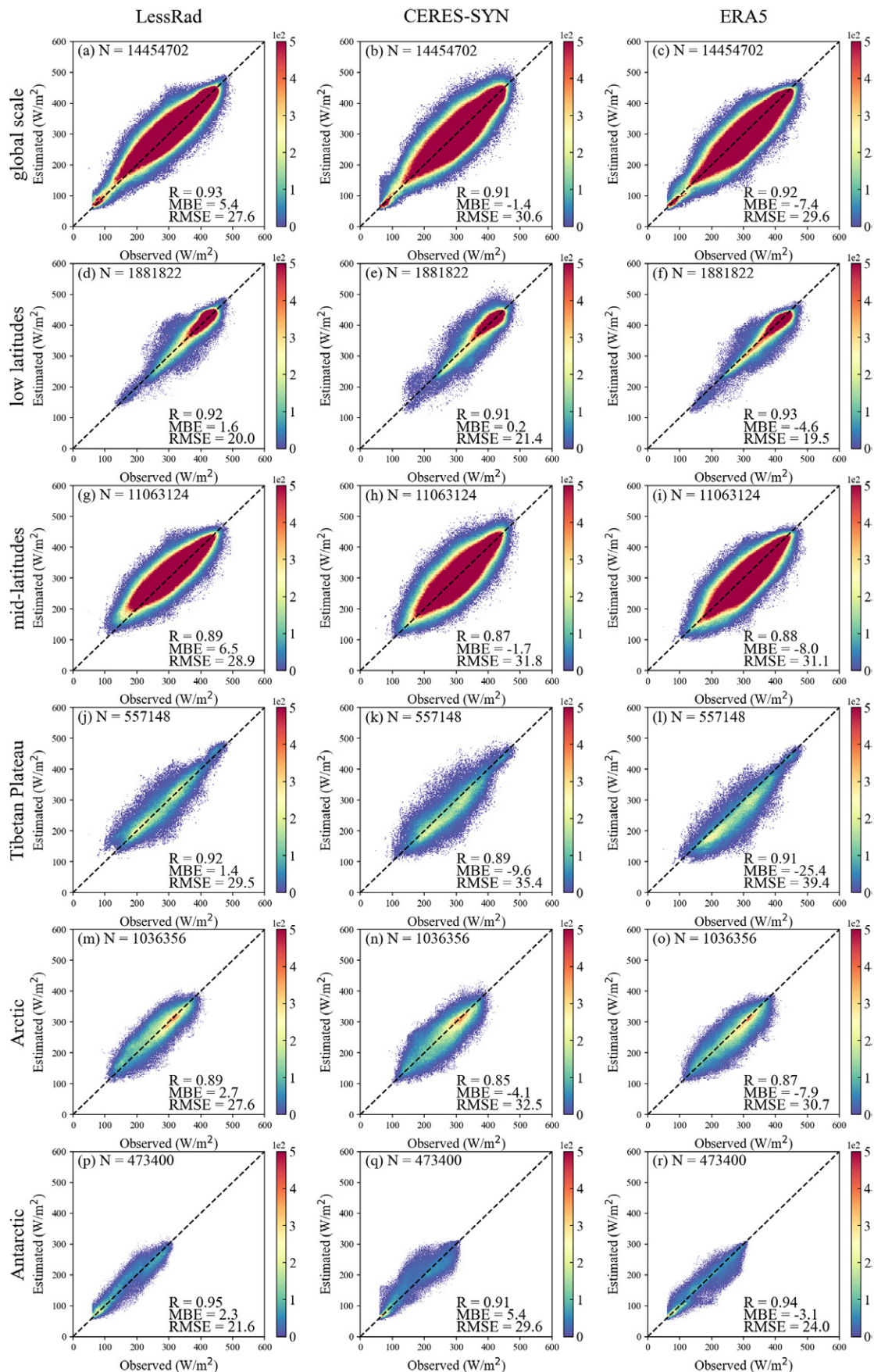
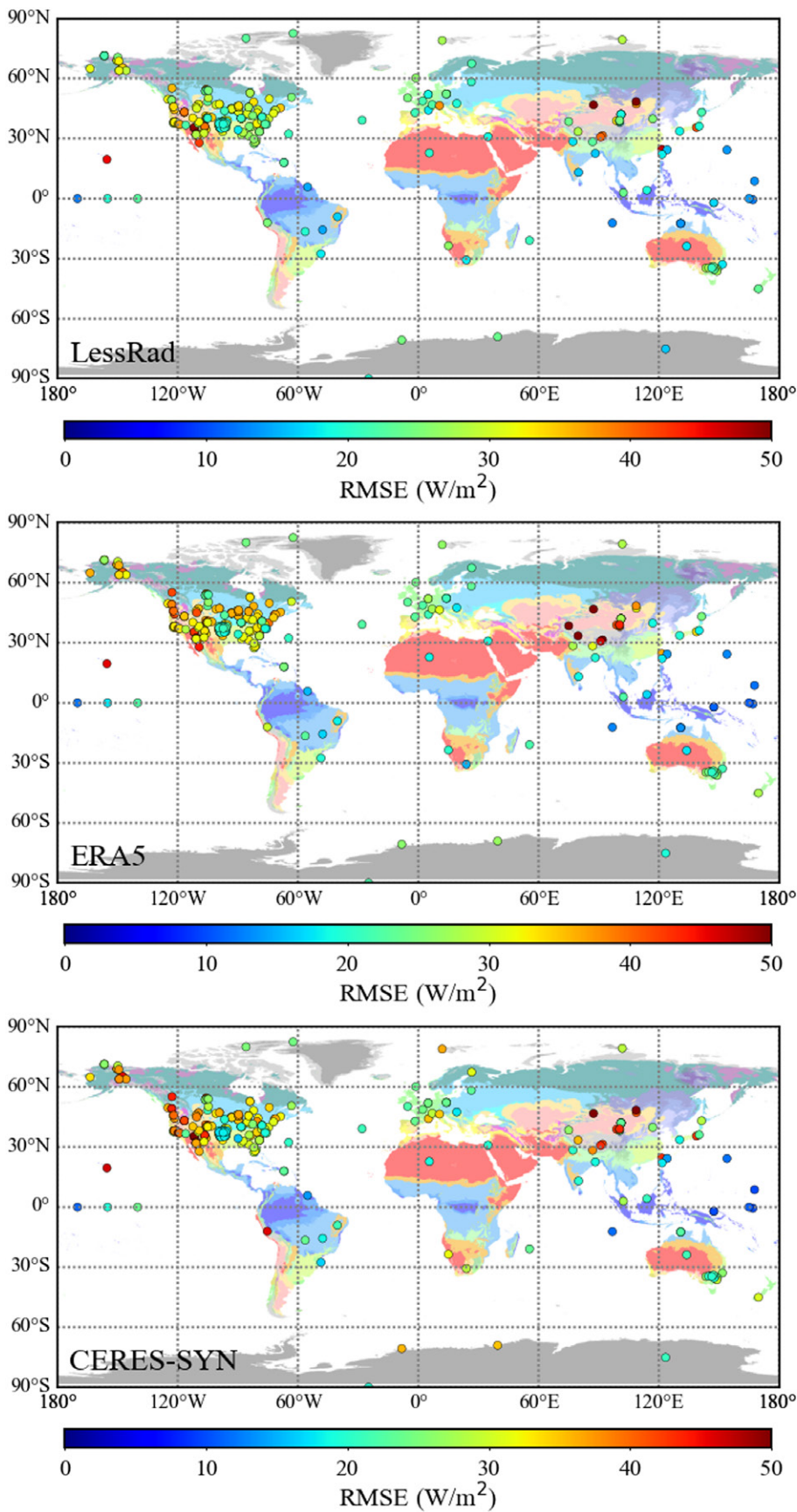


FIG. 8. Comparison of the hourly LWDR results of (left) LessRad, (center) CERES-SYN, and (right) ERA5 with ground-based measurements. The top row depicts global results, while the second to sixth rows show specific regions including low latitudes, midlatitudes, the Tibetan Plateau, the Arctic, and the Antarctic. All products have been resampled to a scale of 1°. MBE and RMSE are expressed in watts per square meter.



Köppen-Geiger climate classification

Af	Cwa	Dwa
Am	Cwb	Dwb
Aw	Cwc	Dwc
BWh	Cfa	Dwd
BWk	Cfb	Dfa
BSh	Cfc	Dfb
BSk	Dsa	Dfc
Csa	Dsb	Dfd
Csb	Dsc	ET
Csc	Dsd	EF

- Af : Tropical, rainforest
- Am : Tropical, monsoon
- Aw : Tropical, savannah
- BWh : Arid, desert, hot
- BWk : Arid, desert, cold
- BSh : Arid, steppe, hot
- BSk : Arid, steppe, cold
- Csa : Temperate, dry summer, hot summer
- Csb : Temperate, dry summer, warm summer
- Csc : Temperate, dry summer, cold summer
- Cwa : Temperate, dry winter, hot summer
- Cwb : Temperate, dry winter, warm summer
- Cwc : Temperate, dry winter, cold summer
- Cfa : Temperate, no dry season, hot summer
- Cfb : Temperate, no dry season, warm summer
- Cfc : Temperate, no dry season, cold summer
- Dsa : Cold, dry summer, hot summer
- Dsb : Cold, dry summer, warm summer
- Dsc : Cold, dry summer, cold summer
- Dsd : Cold, dry summer, very cold winter
- Dwa : Cold, dry winter, hot summer
- Dwb : Cold, dry winter, warm summer
- Dwc : Cold, dry winter, cold summer
- Dwd : Cold, dry winter, very cold winter
- Dfa : Cold, no dry season, hot summer
- Dfb : Cold, no dry season, warm summer
- Dfc : Cold, no dry season, cold summer
- Dfd : Cold, no dry season, very cold winter
- ET : Polar, tundra
- EF : Polar, frost

Fig. 9. The comparison of LWDR RMSE of (top) LessRad, (middle) ERA5, and (bottom) CERES-SYN at various sites and over Köppen-Geiger climatic types.

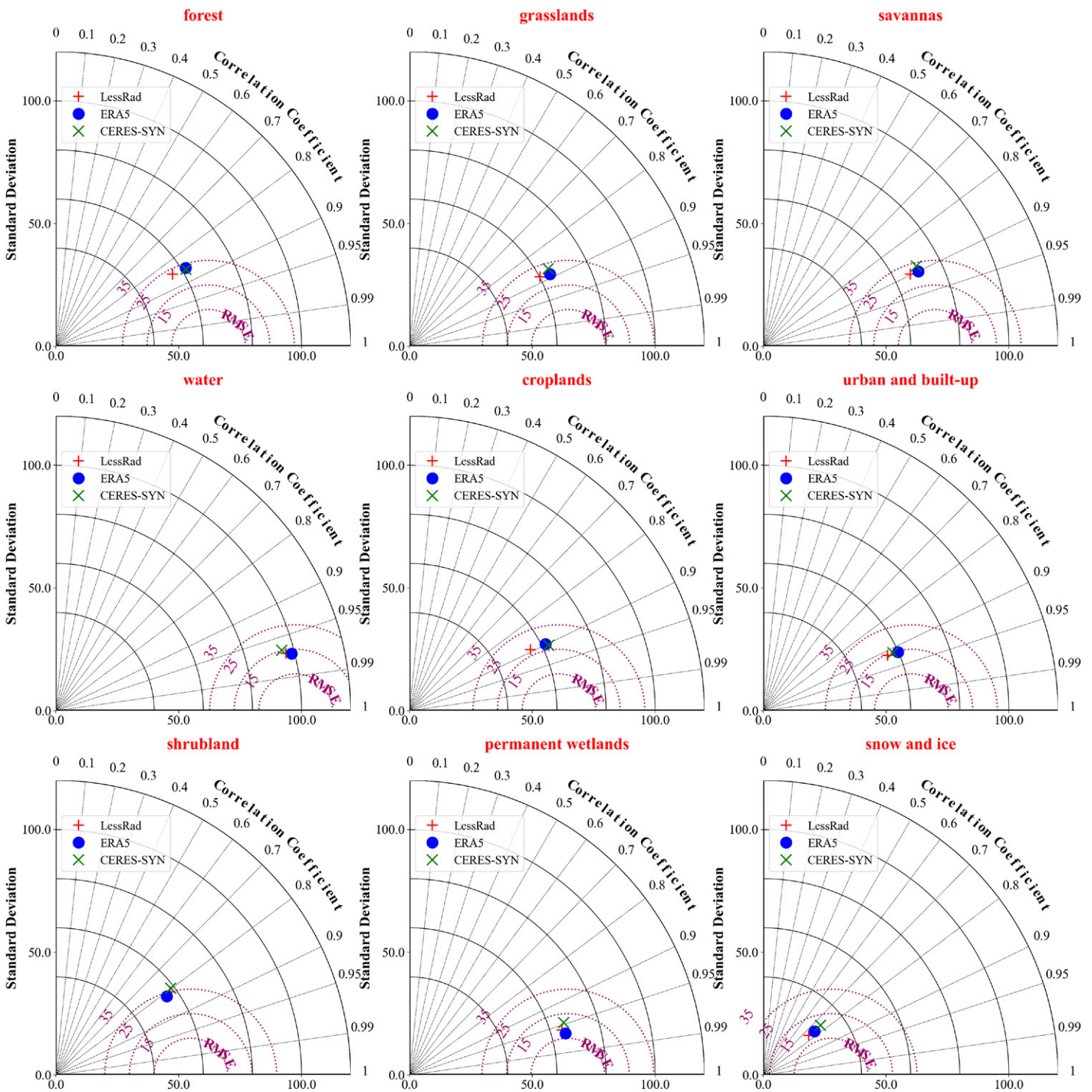


FIG. 10. Comparison of hourly LWDR results on nine major land-cover types between LessRad at 5-km resolution, ERA5 at 0.25° resolution, and CERES-SYN at 1° resolution with ground-based measurements.

higher spatial resolution, LessRad facilitates the fine-scale investigation of surface radiation budgets for different land cover types, enabling long-term quantification of climate impacts with exceptional performance.

6. Conclusions

This study generates an all-sky global LWDR product called LessRad LWDR with high accuracy at 5-km and 1-h resolution based on MODIS data and ERA5 reanalysis hourly data from 2002 to 2022. Unlike existing products, LessRad is estimated based on the instantaneous measurements using a single remote sensing instrument, i.e., MODIS. The main advantages

of this new product are its high spatiotemporal resolution and improved accuracy. The spatial resolution (5 km) of LessRad is greatly higher than that of CERES-SYN (1°) and ERA5 (0.25°), and its accuracy is superior to or at least comparable with these products on both global and regional scales.

LessRad exhibits RMSE values of 29.7, 21.4, 31.0, 32.0, 30.2, and 24.2 W m⁻² over the globe, low latitudes, midlatitudes, the Tibetan Plateau, the Arctic, and the Antarctic, respectively. The comprehensive validation reveals that it shows obvious advantages at the regional scales in terms of both accuracy and spatial pattern, demonstrating its better applicability under complex terrain and various climatic conditions.

This study combines the advantages of MODIS and ERA5, employing the latest all-sky instantaneous LWDR estimation algorithm and temporal upscaling model. It breaks through the defects of satellite-based LWDR estimations which are limited for a long time by cloud and observation frequency, especially for the polar-orbiting satellites. LessRad LWDR deepens the understanding of the LWDR evolution in different areas under global warming, allowing for a more comprehensive and accurate assessment of global LWDR dynamics. It provides a unique data basis for land radiation flux and related processes in fine-scale studies.

Acknowledgments. This work was carried out under the cofunding of the National Natural Science Foundation of China projects (42022008, 42025504, and 42371342), the Innovation Group Project of Southern Marine Science and Engineering Guangdong Laboratory (Zhuhai) (311022003), and the Zhuhai Basic and Applied Basic Research Project (ZH22017003200009PWC).

Data availability statement. The LWDR product has been provided via the National Tibetan Plateau Data Center (<https://doi.org/10.11888/Terre.tpd.300867>; <https://cstr.cn/18406.11.Terre.tpd.300867>).

References

- Andrews, T., P. M. Forster, and J. M. Gregory, 2009: A surface energy perspective on climate change. *J. Climate*, **22**, 2557–2570, <https://doi.org/10.1175/2008JCLI2759.1>.
- Beck, H. E., and Coauthors, 2023: High-resolution (1 km) Köppen-Geiger maps for 1901–2099 based on constrained CMIP6 projections. *Sci. Data*, **10**, 724, <https://doi.org/10.1038/s41597-023-02549-6>.
- Bourassa, M. A., and Coauthors, 2013: High-latitude ocean and sea ice surface fluxes: Challenges for climate research. *Bull. Amer. Meteor. Soc.*, **94**, 403–423, <https://doi.org/10.1175/BAMS-D-11-00244.1>.
- Carmona, F., R. Rivas, and V. Caselles, 2014: Estimation of daytime downward longwave radiation under clear and cloudy skies conditions over a sub-humid region. *Theor. Appl. Climatol.*, **115**, 281–295, <https://doi.org/10.1007/s00704-013-0891-3>.
- Carrer, D., S. Lafont, J.-L. Roujean, J.-C. Calvet, C. Meurey, P. Le Moigne, and I. F. Trigo, 2012: Incoming solar and infrared radiation derived from METEOSAT: Impact on the modeled land water and energy budget over France. *J. Hydro-meteorol.*, **13**, 504–520, <https://doi.org/10.1175/JHM-D-11-059.1>.
- Cheng, J., S. L. Liang, W. H. Wang, and Y. M. Guo, 2017: An efficient hybrid method for estimating clear-sky surface downward longwave radiation from MODIS data. *J. Geophys. Res. Atmos.*, **122**, 2616–2630, <https://doi.org/10.1002/2016JD026250>.
- , F. Yang, and Y. M. Guo, 2019: A comparative study of bulk parameterization schemes for estimating cloudy-sky surface downward longwave radiation. *Remote Sens.*, **11**, 528, <https://doi.org/10.3390/rs11050528>.
- Colman, R. A., 2015: Climate radiative feedbacks and adjustments at the Earth's surface. *J. Geophys. Res. Atmos.*, **120**, 3173–3182, <https://doi.org/10.1002/2014JD022896>.
- Darnell, W. L., S. K. Gupta, and W. F. Staylor, 1986: Downward longwave surface radiation from sun-synchronous satellite data: Validation of methodology. *J. Climate Appl. Meteorol.*, **25**, 1012–1021, [https://doi.org/10.1175/1520-0450\(1986\)025<1012:DLSRFS>2.0.CO;2](https://doi.org/10.1175/1520-0450(1986)025<1012:DLSRFS>2.0.CO;2).
- DeAngelis, A. M., X. Qu, M. D. Zelinka, and A. Hall, 2015: An observational radiative constraint on hydrologic cycle intensification. *Nature*, **528**, 249–253, <https://doi.org/10.1038/nature15770>.
- DeConto, R. M., and D. Pollard, 2016: Contribution of Antarctica to past and future sea-level rise. *Nature*, **531**, 591–597, <https://doi.org/10.1038/nature17145>.
- Doelling, D. R., M. Sun, L. T. Nguyen, M. L. Nordeen, C. O. Haney, D. F. Keyes, and P. E. Mlynczak, 2016: Advances in geostationary-derived longwave fluxes for the CERES synoptic (SYN1deg) product. *J. Atmos. Oceanic Technol.*, **33**, 503–521, <https://doi.org/10.1175/JTECH-D-15-0147.1>.
- Driemel, A., and Coauthors, 2018: Baseline Surface Radiation Network (BSRN): Structure and data description (1992–2017). *Earth Syst. Sci. Data*, **10**, 1491–1501, <https://doi.org/10.5194/essd-10-1491-2018>.
- Du, Y., T. Wang, Y. Zhou, D. Li, S. Wang, and Y. Xian, 2023: Upscaling of longwave downward radiation from instantaneous to any temporal scale: Algorithms, validation, and comparison. *Int. J. Appl. Earth Obs. Geoinf.*, **117**, 103196, <https://doi.org/10.1016/j.jag.2023.103196>.
- Duarte, H. F., N. L. Dias, and S. R. Maggioletto, 2006: Assessing daytime downward longwave radiation estimates for clear and cloudy skies in Southern Brazil. *Agric. For. Meteorol.*, **139**, 171–181, <https://doi.org/10.1016/j.agrformet.2006.06.008>.
- Forman, B. A., and S. A. Margulis, 2009: High-resolution satellite-based cloud-coupled estimates of total downwelling surface radiation for hydrologic modelling applications. *Hydrol. Earth Syst. Sci.*, **13**, 969–986, <https://doi.org/10.5194/hess-13-969-2009>.
- Frouin, R., C. Gautier, and J. J. Morcrette, 1988: Downward longwave irradiance at the ocean surface from satellite data: Methodology and in situ validation. *J. Geophys. Res.*, **93**, 597–619, <https://doi.org/10.1029/JC093iC01p00597>.
- Gelaro, R., and Coauthors, 2017: The Modern-Era Retrospective Analysis for Research and Applications, version 2 (MERRA-2). *J. Climate*, **30**, 5419–5454, <https://doi.org/10.1175/JCLI-D-16-0758.1>.
- Guo, Y., J. Cheng, and S. Liang, 2018: Comprehensive assessment of parameterization methods for estimating clear-sky surface downward longwave radiation. *Theor. Appl. Climatol.*, **135**, 1045–1058, <https://doi.org/10.1007/s00704-018-2423-7>.
- Gupta, S. K., D. P. Kratz, P. W. Stackhouse, A. C. Wilber, T. P. Zhang, and V. E. Sotthcott, 2010: Improvement of surface longwave flux algorithms used in CERES processing. *J. Appl. Meteor. Climatol.*, **49**, 1579–1589, <https://doi.org/10.1175/2010JAMC2463.1>.
- Hersbach, H., and Coauthors, 2020: The ERA5 global reanalysis. *Quart. J. Roy. Meteor. Soc.*, **146**, 1999–2049, <https://doi.org/10.1002/qj.3803>.
- Hu, S. Z., P. C. Hsu, W. K. Li, L. Wang, H. S. Chen, and B. T. Zhou, 2023: Mechanisms of Tibetan Plateau warming amplification in recent decades and future projections. *J. Climate*, **36**, 5775–5792, <https://doi.org/10.1175/JCLI-D-22-0471.1>.
- Iziomon, M. G., H. Mayer, and A. Matzarakis, 2003: Downward atmospheric longwave irradiance under clear and cloudy skies: Measurement and parameterization. *J. Atmos. Sol.-Terr. Phys.*, **65**, 1107–1116, <https://doi.org/10.1016/j.jastp.2003.07.007>.
- Kobayashi, S., and Coauthors, 2015: The JRA-55 reanalysis: General specifications and basic characteristics. *J. Meteor. Soc. Japan*, **93**, 5–48, <https://doi.org/10.2151/jmsj.2015-001>.
- Letu, H., and Coauthors, 2022: A new benchmark for surface radiation products over the East Asia-Pacific region retrieved from the Himawari-8/AHI next-generation geostationary satellite. *Bull. Amer. Meteor. Soc.*, **103**, E873–E888, <https://doi.org/10.1175/BAMS-D-20-0148.1>.
- Lhomme, J. P., J. J. Vacher, and A. Rocheteau, 2007: Estimating downward longwave radiation on the Andean Altiplano. *Agric. For. Meteorol.*, **145**, 139–148, <https://doi.org/10.1016/j.agrformet.2007.04.007>.
- Li, X., and Coauthors, 2013: Heihe Watershed Allied Telemetry Experimental Research (HiWATER): Scientific objectives and experimental design. *Bull. Amer. Meteor. Soc.*, **94**, 1145–1160, <https://doi.org/10.1175/BAMS-D-12-00154.1>.
- Liang, S. L., and Coauthors, 2021: The Global Land Surface Satellite (GLASS) product suite. *Bull. Amer. Meteor. Soc.*, **102**, E323–E337, <https://doi.org/10.1175/BAMS-D-18-0341.1>.
- Lin, H., Z. L. Li, J. Li, F. Zhang, M. Min, and W. P. Menzel, 2022: Estimate of daytime single-layer cloud base height from advanced baseline imager measurements. *Remote Sens. Environ.*, **274**, 112970, <https://doi.org/10.1016/j.rse.2022.112970>.
- Loeb, N. G., G. C. Johnson, T. J. Thorsen, J. M. Lyman, F. G. Rose, and S. Kato, 2021: Satellite and ocean data reveal marked increase in Earth's heating rate. *Geophys. Res. Lett.*, **48**, e2021GL093047, <https://doi.org/10.1029/2021GL093047>.
- Ma, Q., K. C. Wang, and M. Wild, 2014: Evaluations of atmospheric downward longwave radiation from 44 coupled general circulation models of CMIP5. *J. Geophys. Res. Atmos.*, **119**, 4486–4497, <https://doi.org/10.1002/2013JD021427>.
- Ma, Y., and Coauthors, 2020: A long-term (2005–2016) dataset of hourly integrated land-atmosphere interaction observations on the Tibetan Plateau. *Earth Syst. Sci. Data*, **12**, 2937–2957, <https://doi.org/10.5194/essd-12-2937-2020>.
- Mangum, L. J., H. P. Freitag, and M. J. McPhaden, 1994: TOGA-TAO array sampling schemes and sensor evaluations. *Proc. OCEANS'94*, Brest, France, NOAA, II/402–II/406, <https://doi.org/10.1109/OCEANS.1994.364077>.
- Mizoguchi, Y., A. Miyata, Y. Ohtani, R. Hirata, and S. Yuta, 2009: A review of tower flux observation sites in Asia. *J. For. Res.*, **14** (1), 1–9, <https://doi.org/10.1007/s10310-008-0101-9>.
- Muñoz-Sabater, J., and Coauthors, 2021: ERA5-Land: A state-of-the-art global reanalysis dataset for land applications. *Earth Syst. Sci. Data*, **13**, 4349–4383, <https://doi.org/10.5194/essd-13-4349-2021>.
- Noh, Y. J., and Coauthors, 2017: Cloud-base height estimation from VIIRS. Part II: A statistical algorithm based on A-Train satellite data. *J. Atmos. Oceanic Technol.*, **34**, 585–598, <https://doi.org/10.1175/JTECH-D-16-0110.1>.
- Nussbaumer, E. A., and R. T. Pinker, 2012: Estimating surface longwave radiative fluxes from satellites utilizing artificial neural networks. *J. Geophys. Res.*, **117**, D07209, <https://doi.org/10.1029/2011JD017141>.

- Platnick, S., and Coauthors, 2017: The MODIS cloud optical and microphysical products: Collection 6 updates and examples from Terra and Aqua. *IEEE Trans. Geosci. Remote Sens.*, **55**, 502–525, <https://doi.org/10.1109/TGRS.2016.2610522>.
- Previdi, M., and B. G. Liepert, 2012: The vertical distribution of climate forcings and feedbacks from the surface to top of atmosphere. *Climate Dyn.*, **39**, 941–951, <https://doi.org/10.1007/s00382-011-1233-8>.
- Rutan, D. A., S. Kato, D. R. Doelling, F. G. Rose, L. T. Nguyen, T. E. Caldwell, and N. G. Loeb, 2015: CERES synoptic product: Methodology and validation of surface radiant flux. *J. Atmos. Oceanic Technol.*, **32**, 1121–1143, <https://doi.org/10.1175/JTECH-D-14-00165.1>.
- Saha, S., and Coauthors, 2010: The NCEP Climate Forecast System Reanalysis. *Bull. Amer. Meteor. Soc.*, **91**, 1015–1058, <https://doi.org/10.1175/2010BAMS3001.1>.
- , and Coauthors, 2014: The NCEP Climate Forecast System version 2. *J. Climate*, **27**, 2185–2208, <https://doi.org/10.1175/JCLI-D-12-00823.1>.
- Schmidt, A., C. Hanson, W. S. Chan, and B. E. Law, 2012: Empirical assessment of uncertainties of meteorological parameters and turbulent fluxes in the AmeriFlux network. *J. Geophys. Res.*, **117**, G04014, <https://doi.org/10.1029/2012JG002100>.
- Screen, J. A., and I. Simmonds, 2010: The central role of diminishing sea ice in recent Arctic temperature amplification. *Nature*, **464**, 1334–1337, <https://doi.org/10.1038/nature09051>.
- Shao, J. Q., H. Letu, X. Ri, G. Tana, T. X. Wang, and H. Z. Shang, 2023: Estimation of surface downward longwave radiation and cloud base height based on infrared multichannel data of Himawari-8. *Atmosphere*, **14**, 493, <https://doi.org/10.3390/atmos14030493>.
- Shunlin, L., and Coauthors, 2023: Updates on Global LAnd Surface Satellite (GLASS) products suite. *Natl. Remote Sens. Bull.*, **27**, 831–856, <https://doi.org/10.11834/jrs.20232462>.
- Tamagawa, K., M. Kitsuregawa, E. Ikoma, T. Ohta, S. Williams, and T. Koike, 2008: An advanced quality control system for the CEOP/CAMP in-situ data management. *IEEE Syst. J.*, **2**, 406–413, <https://doi.org/10.1109/JSYST.2008.927710>.
- Wang, G., T. Wang, and H. Xue, 2021: Validation and comparison of surface shortwave and longwave radiation products over the three poles. *Int. J. Appl. Earth Obs. Geoinf.*, **104**, 102538, <https://doi.org/10.1016/j.jag.2021.102538>.
- Wang, K. C., and R. E. Dickinson, 2013: Global atmospheric downward longwave radiation at the surface from ground-based observations, satellite retrievals, and reanalyses. *Rev. Geophys.*, **51**, 150–185, <https://doi.org/10.1002/rog.20009>.
- Wang, T., and Coauthors, 2018: Cloudy-sky land surface longwave downward radiation (LWDR) estimation by integrating MODIS and AIRS/AMSU measurements. *Remote Sens. Environ.*, **205**, 100–111, <https://doi.org/10.1016/j.rse.2017.11.011>.
- , J. Shi, Y. Ma, H. Letu, and X. Li, 2020: All-sky longwave downward radiation from satellite measurements: General parameterizations based on LST, column water vapor and cloud top temperature. *ISPRS J. Photogramm. Remote Sens.*, **161**, 52–60, <https://doi.org/10.1016/j.isprsjrs.2020.01.011>.
- , G. Wang, C. Shi, Y. Du, H. Letu, W. Zhang, and H. Xue, 2023: Improved algorithm to derive all-sky longwave downward radiation from space: Application to Fengyun-4A measurements. *IEEE Trans. Geosci. Remote Sens.*, **61**, 1–13, <https://doi.org/10.1109/TGRS.2023.3289058>.
- Wang, W. H., and S. L. Liang, 2009: Estimation of high-spatial resolution clear-sky longwave downward and net radiation over land surfaces from MODIS data. *Remote Sens. Environ.*, **113**, 745–754, <https://doi.org/10.1016/j.rse.2008.12.004>.
- , and —, 2010: A method for estimating clear-sky instantaneous land-surface longwave radiation with GOES sounder and GOES-R ABI data. *IEEE Geosci. Remote Sens. Lett.*, **7**, 708–712, <https://doi.org/10.1109/LGRS.2010.2046472>.
- Wild, M., 2016: Decadal changes in radiative fluxes at land and ocean surfaces and their relevance for global warming. *Wiley Interdiscip. Rev.: Climate Change*, **7**, 91–107, <https://doi.org/10.1002/wcc.372>.
- Xu, J., S. Liang, H. Ma, T. He, Y. Zhang, and G. Zhang, 2023: A daily 5-km all-sky sea-surface longwave radiation product based on statistically modified deep neural network and spatiotemporal analysis for 1981–2018. *Remote Sens. Environ.*, **290**, 113550, <https://doi.org/10.1016/j.rse.2023.113550>.
- Yang, J., Z. Q. Zhang, C. Y. Wei, F. Lu, and Q. Guo, 2017: Introducing the new generation of Chinese geostationary weather satellites, Fengyun-4. *Bull. Amer. Meteor. Soc.*, **98**, 1637–1658, <https://doi.org/10.1175/BAMS-D-16-0065.1>.
- Zhou, Y. P., and R. D. Cess, 2001: Algorithm development strategies for retrieving the downwelling longwave flux at the Earth's surface. *J. Geophys. Res.*, **106**, 12 477–12 488, <https://doi.org/10.1029/2001JD900144>.
- , D. P. Kratz, A. C. Wilber, S. K. Gupta, and R. D. Cess, 2007: An improved algorithm for retrieving surface downwelling longwave radiation from satellite measurements. *J. Geophys. Res.*, **112**, D15102, <https://doi.org/10.1029/2006JD008159>.
- Zhu, F., X. Li, J. Qin, K. Yang, L. Cuo, W. Tang, and C. Shen, 2022: Integration of multisource data to estimate downward longwave radiation based on deep neural networks. *IEEE Trans. Geosci. Remote Sens.*, **60**, 1–12, <https://doi.org/10.1109/TGRS.2022.3230829>.